

## Analysis of depinning behavior of drop on chemically heterogeneous surface

Bing He,<sup>1,2</sup> Chunyan Qin,<sup>1</sup> Sihao Zhou,<sup>1</sup> and Binghai Wen<sup>1,2,\*</sup>

<sup>1</sup>*College of Computer Science and Information Engineering, Guangxi Normal University, Guilin 541004, China*

<sup>2</sup>*Guangxi Key Lab of Multi-source Information Mining & Security, Guangxi Normal University, Guilin 541004, China*



(Received 27 March 2020; accepted 9 October 2020; published 13 November 2020)

The depinning behavior of a drop on an inclined heterogeneous surface comprising hydrophilic-hydrophobic stripes is investigated by the multiphase lattice Boltzmann method driven by the chemical potential. Different initial states of the drop lead to three types of depinning behavior. When the drop is initially in the moderate state, the front and rear contact angles linearly change as the slope angle continues to increase, and depinning almost simultaneously occurs at the front and rear contact lines. Unilateral depinning occurs at the front contact line for the contracted state and at the rear contact line for the elongated state, with sudden instabilities of the contact angle. It is clearly observed that the unilateral depinning process consists of a slow-moving process and a fast-moving process. The dynamic equilibrium reflects the competition between gravity and the capillary force in the whole drop. At the microscopic scale, based on measurement of the real-time contact angle, it is illustrated that the local force balance in the contact line region is maintained by the unbalanced Young's force and the resistance of the substrate in the slow-moving stage, while the unbalanced Young's force provides the driving force for the motion of the contact line in the fast-moving stage.

DOI: [10.1103/PhysRevFluids.5.114003](https://doi.org/10.1103/PhysRevFluids.5.114003)

### I. INTRODUCTION

Controlling and predicting the motion of liquid drops in contact with a heterogeneous substrate has wide technological implications in many areas, such as microfluidics [1], self-cleaning [2], cooling [3], and water collection [4]. These applications require insight into the behavior at the moment that the drops start sliding over realistic substrates [5,6]. The wettability of the substrate is a crucial factor for determining the stability and dynamics of a drop. Especially on chemically heterogeneous substrates, several issues associated with the complicated contact line behavior and force balance have attracted much attention [7,8]. Despite tremendous research effort, many aspects of the stability and dynamics of drops are still not well understood. Much attention has been paid to the drop sliding [9–15] and depinning behavior [16–23] on chemically heterogeneous surfaces.

Several studies have revealed the effect of chemically patterned surfaces on the drop sliding behavior. For linear chemical patterns (stripes), Morita *et al.* [9] analyzed and compared the anisotropy behavior of drops sliding on the stripe-patterned surface in different directions (parallel and orthogonal to the stripe direction). Suzuki *et al.* [10] experimentally investigated the drop sliding behavior on stripe-patterned hydrophobic surfaces. They observed and analyzed the effect of the rotation angle on the sliding behavior by changing the stripe direction with respect to the slope direction. Sbragaglia *et al.* [11,12] demonstrated a stick-slip drop sliding behavior on a chemically

---

\*oceanwen@gxnu.edu.cn

heterogeneous stripe-patterned surface by theoretical and experimental methods. They found that the sliding speed of a drop on a chemically heterogeneous surface is significantly slower than that on a homogeneous surface and reproduced the stick-slip motion of the drop by the lattice Boltzmann model (LBM) [11]. The physical mechanisms behind the sliding dynamics were explained by analyzing the calculated balance of the capillary, viscous, and body forces; the surface composition; and the liquid viscosity [12]. Wang *et al.* [13] observed the drop motion on a stripe-patterned surface by setting the drop aspect ratio, deposition position, and body force direction. In addition to stripe-patterned surfaces, drop sliding has also been observed on chessboard-patterned surfaces [14,15]. There is no doubt that the substrate heterogeneity can act as an energy barrier to resist drop motion.

Understanding the transient depinning behavior of drops is crucial for controlling the motion of liquid drops on chemically heterogeneous surfaces. It has been found that depinning behavior might occur from either the front or rear contact line [16–23].

Thiele and Knobloch [16] studied the depinning process of drops moving over a wettability defect using the thin-film model. Berejnov and Thorne [17] analyzed the stability of drops pinned on a hydrophobic inclined plane by experiment. Three transitions of partial depinning were observed in their experiments. Chou *et al.* [18] analyzed the relations between the initial contact angle and the depinning behavior of a tilted drop by experimental and numerical methods. They observed that if the initial contact angle is set to be equal to the advancing contact angle, the front contact line moves, while the rear contact line is still pinned. Conversely, if the initial contact angle is set to the receding contact angle, the rear contact line moves and the front contact line is still pinned. They also analyzed the variation of free energy with shape deformation by SURFACE EVOLVER which evolves the surfaces shaped by total free energy toward a local minimum energy. Santos *et al.* [19] developed a new method for dealing with contact angle hysteresis in SURFACE EVOLVER, and simulated the liquid drops on inclined surfaces by this method. They found that the front contact angle increases and the rear contact angle decreases at similar rates if the initial contact angle is set to the mean of the advancing and receding contact angles. Bommer *et al.* [20] investigated the depinning behavior of liquid drops with different sizes and surface tensions by experiments and LBM simulations. However, they did not discuss the drop motion after depinning. Following the same approach as described in [19], Janardan and Panchagnula [21] found that two critical inclination angles, the moving and sliding angles, describe the incipient motion of the drop. White *et al.* [22] analyzed the evolution of the contact angles by SURFACE EVOLVER calculations and evaluated the most stable contact angle for tilted drops. In addition, Herde *et al.* [23] studied the depinning of droplets with large contact angles on a sinusoidal wettability pattern by solving the Stokes equation. They found that the substrate properties and the slip length strongly affect the depinning dynamics.

A large number of studies have analyzed the initial contact angle of a drop that induces depinning behavior and determined the variation of the critical inclination angle. Recently, the capillary force in the depinning process has also been discussed. Gao *et al.* [5] measured the capillary force between a drop and a solid substrate. Sarshar *et al.* [24] analyzed the depinning force of receding drops on pillared superhydrophobic surfaces. However, the physical descriptions of the onset of drop depinning remain incomplete, particularly in relation to the contact line behavior on chemically heterogeneous substrates.

Modeling the contact line dynamics is an essential part of simulating and analyzing the depinning process. In recent years, various methods have been employed to treat moving contact lines. The local constraints in the triple contact line are added to SURFACE EVOLVER for controlling the motion of the contact line and modeling contact angle hysteresis [19,21,22]. Thus, a hysteresis surface is characterized by use of only two parameters: the advancing and receding contact angles. This approach is not adequate for the specific and complex heterogeneous surface. Herde *et al.* [23] studied the depinning of droplets by employing the Navier slip boundary condition. This calculation that needs first to determine the curvature by SURFACE EVOLVER and then adds the slip boundary condition to the contact line is very complex, and the viscosity of the vapor phase is neglected in their model. Thiele and collaborators [16,25] analyzed the contact line motion on a heterogeneous

substrate by using a disjoining pressure on a precursor film. The drawback of this method is that it restricts analysis to a droplet with small contact angles. The diffuse interface method is widely implemented in multiphase flow lattice Boltzmann models [11,12,26–30], in which the contact line moves along with a phase transition or diffusion [31,32]. Based on the mesoscopic scale, LBM can simulate the interaction between different phases and handle the complex interfacial deformation without the interface tracking [33–35], and LBM-based models are easier to implement than the conventional computational models.

The depinning behavior depends on the initial conditions of the system corresponding to different metastable states. Marmur and collaborators studied contact angle hysteresis of a drop on a chemically heterogeneous surface by numerical methods and discussed the dependence of the contact angle on the change of the volume [36–39]. They found that the number of equilibrium drops is either fixed or increases with growing volume, even on the same surface [38]. Based on observation in the energy landscape, Herde *et al.* [23] found three different types of equilibrium states of drops which depend on the substrate properties. When drops are deposited on heterogeneous surfaces with different length ratios or different deposition positions, the drops are in different states [13]. Many factors result in the multiple metastable states of the drop, including volume, substrate property, and deposition position.

The aim of this study is to shed light on the depinning behavior of drops with different initial states on a chemically heterogeneous surface by the multiphase LBM. A two-dimensional water-vapor system model was built by the chemical-potential multiphase method [30,40]. The chemically heterogeneous surface can be easily modeled by the chemical-potential boundary condition. The depinning process was simulated in detail and the effect of the initial state was investigated. Accurate real-time contact angles were obtained by the mesoscopic measurement method [41], which captured the transient variation of the front and rear contact angles of the drop in the depinning process and the transfer of the drop from one metastable state to another when unilateral depinning occurs. This also aids in on-the-spot analysis of the overall force balance and the changes of the local force at the front and rear contact lines.

## II. NUMERICAL METHOD

### A. Multiphase model driven by the chemical potential

The LBM originates from the lattice gas automaton concept and kinetic theory [42,43]. Several variations of the lattice Boltzmann equation have been derived with different collision operators, such as the Bhatnagar-Gross-Krook model [44], the multiple-relaxation-time model [45], and the entropic-based model [46]. Fully discretized in space, time, and velocity, the lattice Boltzmann equation with a single relaxation time can be expressed as

$$f_i(\mathbf{x} + \mathbf{e}_i, t + 1) - f_i(\mathbf{x}, t) = -\frac{1}{\tau} [f_i(\mathbf{x}, t) - f_i^{(\text{eq})}(\mathbf{x}, t)], \quad (1)$$

where  $\tau$  is the relaxation factor,  $\mathbf{e}_i$  are the set of discrete speeds ( $i = 0, \dots, N$ ), and  $f_i(\mathbf{x}, t)$  represents the particle distribution function at lattice site  $\mathbf{x}$  and time  $t$ .  $f_i^{(\text{eq})}$  is the equilibrium distribution function,

$$f_i^{(\text{eq})}(\mathbf{x}, t) = \omega_i \rho \left[ 1 + 3(\mathbf{e}_i \cdot \mathbf{u}) + \frac{9}{2}(\mathbf{e}_i \cdot \mathbf{u})^2 - \frac{3}{2}u^2 \right], \quad (2)$$

where  $\omega_i$  is the weighting coefficient and  $\mathbf{u}$  is the fluid velocity.

Multiphase flow simulations are considered to be the most successful applications of the LBM. The nonideal effects can be calculated from the thermodynamics. From classical capillarity theory by van der Waals, the free-energy functional within the gradient-squared approximation is

[29,47,48]

$$\Psi = \int \Phi d\mathbf{x} = \int \left[ \psi(\rho) + \frac{\kappa}{2} |\nabla \rho|^2 \right] d\mathbf{x}, \quad (3)$$

where  $\psi$  is the bulk free-energy density at a given temperature,  $\rho$  is the local density, and  $\kappa$  is the surface tension coefficient. The square of the gradient term represents the contribution of the free energy from the density gradients in an inhomogeneous system. The chemical potential can be defined by the free-energy density functional [47,49,50]:

$$\mu = \frac{\partial \Phi}{\partial \rho} - \nabla \cdot \frac{\partial \Phi}{\partial (\nabla \rho)} = \psi'(\rho) - \kappa \nabla^2 \rho. \quad (4)$$

The thermodynamic pressure is related to free energy by

$$p(\mathbf{x}) = p_0 - \kappa \rho \nabla^2 \rho - \frac{\kappa}{2} |\nabla \rho|^2, \quad (5)$$

where the equation of state (EOS) can generally be expressed as

$$p_0 = \rho \psi'(\rho) - \psi(\rho). \quad (6)$$

The full pressure tensor of nonuniform fluids contains the nondiagonal terms,

$$P_{\alpha\beta}(\mathbf{x}) = p(\mathbf{x})\delta_{\alpha\beta} + \kappa \frac{\partial \rho}{\partial x_\alpha} \frac{\partial \rho}{\partial x_\beta}, \quad (7)$$

where  $\delta_{\alpha\beta}$  is the Kronecker delta function. The excess pressure can be directly calculated with respect to the ideal gas [29,51]:

$$\mathbf{F}(\mathbf{x}) = -\nabla \cdot \vec{\vec{P}}(\mathbf{x}) + \nabla \cdot \vec{\vec{P}}_0(\mathbf{x}), \quad (8)$$

where  $\vec{\vec{P}}_0 = c_s^2 \rho \vec{\vec{I}}$  is the ideal-gas pressure tensor. Substituting Eqs. (4)–(7) into Eq. (8), the divergence of the pressure tensor is transformed into the gradient of the chemical potential:

$$\mathbf{F}(\mathbf{x}) = -\rho \nabla \mu + \nabla \cdot \vec{\vec{P}}_0(\mathbf{x}). \quad (9)$$

The nonideal force is included within the lattice Boltzmann framework through changing the velocity in the equilibrium distribution function:

$$\mathbf{u}^{\text{eq}} = \mathbf{u} + \frac{\tau \mathbf{F}}{\rho}. \quad (10)$$

The macroscopic velocity of the fluid is redefined by the average momentum before and after particle collision:

$$\mathbf{v} = \mathbf{u} + \frac{\mathbf{F}}{2\rho}. \quad (11)$$

It has been verified that the multiphase LBM driven by the chemical potential satisfies the thermodynamics and Galilean invariance [29,30]. The chemical-potential boundary condition can effectively express the wettability of the chemically heterogeneous surface, on which the dynamic contact angle can be measured on the spot by the mesoscopic scheme [41].

In this study, the popular water-vapor system is constrained by the Peng-Robinson (PR) EOS

$$p_0 = \frac{\rho RT}{1 - b\rho} - \frac{a\alpha\rho^2}{1 + 2b\rho - b^2\rho^2}, \quad (12)$$

where the temperature function is  $\alpha(T) = [1 + (0.37464 + 1.54226\omega - 0.26992\omega^2) \times (1 - \sqrt{T/T_c})]^2$  with acentric factor  $\omega = 0.344$  for water. The parameters are  $a = 2/49$ ,  $b = 2/21$ ,

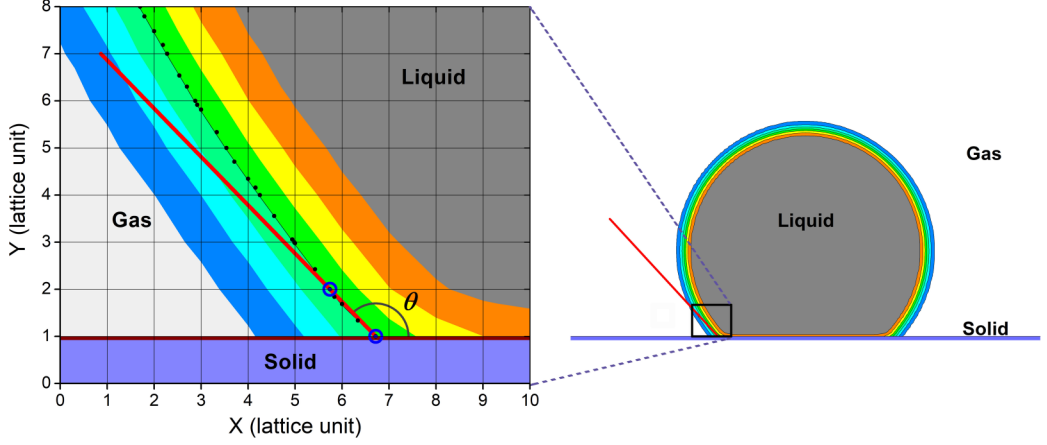


FIG. 1. Schematic diagram of the chemical-potential boundary condition and mesoscopic measurement of the contact angle.

and  $R = 1$ , so the critical temperature is  $T_c = 0.07292$  and the critical density is  $\rho_c = 2.65730$ . The chemical potential of PR EOS is [30]

$$\mu = RT \ln \frac{\rho}{1 - b\rho} - \frac{a\alpha}{2\sqrt{2}b} \ln \frac{\sqrt{2} - 1 + b\rho}{\sqrt{2} + 1 - b\rho} + \frac{RT}{1 - b\rho} - \frac{a\alpha\rho}{1 + 2b\rho - b^2\rho^2} - \kappa \nabla^2 \rho. \quad (13)$$

In an effort to connect the numerical simulations to the real physical systems, the following simulations use the reduced variables  $T_r = T/T_c$  and  $\rho_r = \rho/\rho_c$ . Unless otherwise stated, the following temperature and density refer to the reduced temperature and reduced density, respectively.

In the model, based on the chemical-potential boundary condition [30], the wettability, namely, the interaction between the fluid and solid, is expressed by endowing a solid surface with a specific chemical potential. It influences the nonideal force on fluid-solid interfacial fluid nodes by Eq. (9). Then, this force is incorporated into the lattice Boltzmann framework by Eq. (10).

### B. Contact angle measurement

A planar interface is located at the  $y = 1$  row of lattice nodes and these nodes are treated as fluid nodes (Fig. 1). The distribution functions from the surface are computed by the bounce-back boundary condition. To evaluate the gradient of the lattice nodes, the densities of the solid nodes ( $y = 0$ ) are calculated by the simple weighted average of the fluid densities of the neighbor sites:

$$\rho(x, 0) = \frac{2}{3}\rho(x, 1) + \frac{1}{6}\rho(x-1, 1) + \frac{1}{6}\rho(x+1, 1). \quad (14)$$

The mesoscopic contact angle is defined by the liquid-gas interface and the substrate at the triple-phase contact point [41]. The accurate position of the drop surface on a liquid-gas link is computed by linear interpolation:

$$\mathbf{x} = \mathbf{x}_g + \frac{\rho_m - \rho(\mathbf{x}_g)}{\rho(\mathbf{x}_l) - \rho(\mathbf{x}_g)} \mathbf{e}, \quad (15)$$

where  $\mathbf{x}_l$  and  $\mathbf{x}_g$  are the liquid and gas lattice sites connected by a liquid-gas link,  $\rho_m$  is the average density of the liquid and gas phases, and  $\mathbf{e}$  represents the link direction from the gas to the liquid. A series of discrete points on the drop surface is shown in Fig. 1. The point at  $y = 1$  on the solid surface is considered to be the triple-phase contact point. The point at  $y = 2$  is selected to determine the tangent line of the drop surface at the triple-phase contact point (red line in Fig. 1). The contact

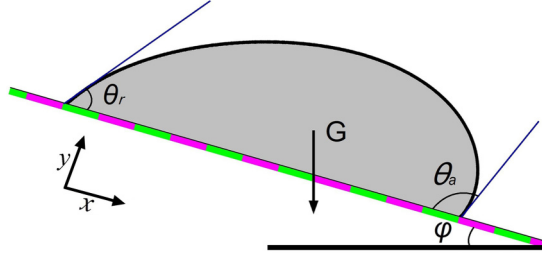


FIG. 2. Schematic diagram of a drop on an inclined heterogeneous surface comprising hydrophilic-hydrophobic stripes. Green segments represent hydrophilic regions, while pink segments represent hydrophobic regions. With gravity  $G$  and slope angle  $\varphi$ , the drop has a front contact angle  $\theta_a$  and a rear contact angle  $\theta_r$ .

angle  $\theta$  is represented by the tangent line and the horizontal positive direction, and its value can be easily calculated by an arctan function.

### C. Drop motion modeling

Considering a sessile drop in contact with an inclined and chemically heterogeneous substrate (Fig. 2), the gravity force  $G$  together with the resistance forces makes the drop deform and balance. In Fig. 2,  $\varphi$  is the slope angle of substrate;  $\theta_a$  and  $\theta_r$ , which are called the front and rear contact angles, are dynamic contact angles at the front and rear ends of the drop, respectively. It should be emphasized that  $\theta_a$  and  $\theta_r$  are different from the advancing and receding angles  $\theta_A$  and  $\theta_R$ , which are the critical values. The chemically heterogeneous surface is patterned with hydrophobic and hydrophilic stripes, as shown in Fig. 2. The green segments represent hydrophilic regions, while the pink segments represent hydrophobic regions. In this situation, the resistance forces are related to the surface inhomogeneity. The motion characteristics of the drop are determined by balancing of the gravitational force and resistance forces, which include the capillary force and viscous force [12].

The simulations are performed on a rectangular domain, with a width of 500 lattice units and a height of 300 lattice units. The diameter of the drop is 120 lattice units, which corresponds to 0.3 mm at the macroscopic scale. The other parameters are temperature  $T = 0.85$ ; the density of the liquid and gas  $\rho_l = 6.63$ ,  $\rho_g = 0.34$ ; surface tension coefficient  $\kappa = 0.01$ ; corresponding surface tension  $\gamma = 0.331$ . When temperature  $T = 0.85$ , the Cahn number that is the ratio of interface thickness and drop radius corresponds to 0.078. The chemical-potential boundary condition [30] is used to express the wettability of the substrate. The substrate is patterned with hydrophilic and hydrophobic stripes, with contact angles of  $60^\circ$  and  $120^\circ$ , respectively. The stripe width is 20 lattice units. Periodic boundary conditions are applied on the left and right sides. Initially, a circular drop falls onto the substrate. Because the corresponding capillary length is 68 lattice units, which is close to the radius of the drop, a symmetric spherical drop can be obtained and gravitational effects are not neglected. After the drop is deposited and reaches its equilibrium state, the substrate is very slowly tilted.

Just before a drop starts to move owing to an increase in the slope angle  $\varphi$ , the front and rear contact angles ( $\theta_a$  and  $\theta_r$ ) leave the initial equilibrium values and are no longer symmetric. Generally, drop destabilization is accompanied by an increase in the front contact angle and a decrease in the rear end contact angle. For a large slope angle, depinning of either the front or rear contact line can occur. The depinning behavior depends on the initial conditions of the system. There are three critical values in the depinning process [17,18,21]. First, when  $\varphi$  reaches the critical value  $\varphi_A$ , the front contact line will locally advance over the substrate. Second, when  $\varphi$  reaches the critical value  $\varphi_R$ , the rear contact line will locally recede [52]. Third, when  $\varphi$  reaches the critical value  $\varphi_C$ , depinning of the front and rear contact lines almost simultaneously occurs and the drop begins to slide.

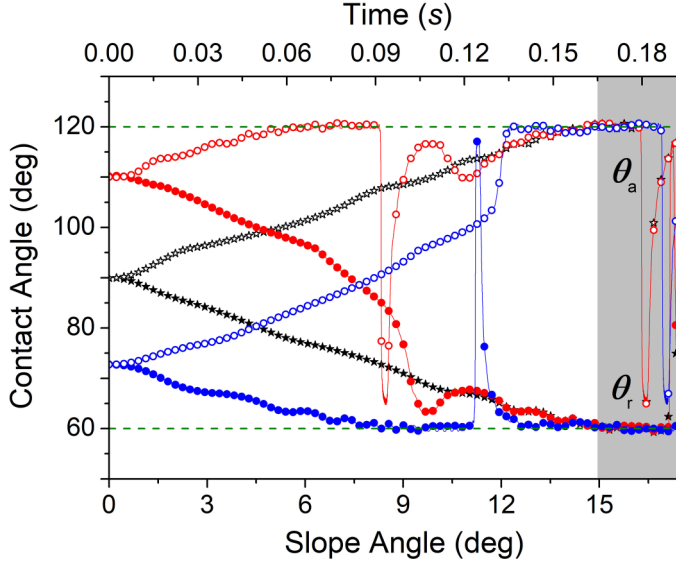


FIG. 3. Comparison of the variations of  $\theta_a$  (open symbols) and  $\theta_r$  (solid symbols) for the (i) moderate state ( $\theta_{\text{int}} = 90^\circ$ , black stars), (ii) contracted state ( $\theta_{\text{int}} = 110^\circ$ , red circles), and (iii) elongated state ( $\theta_{\text{int}} = 72^\circ$ , blue circles). The green dotted lines indicate that the advancing and receding angles  $\theta_A$  and  $\theta_R$  are  $120^\circ$  and  $60^\circ$ , respectively.

### III. RESULTS AND DISCUSSION

#### A. Depinning behavior of drops with different initial states

When drops are deposited on heterogeneous surfaces with different length ratios or different deposition positions, the drops are in different states [13]. There are multiple states with various equilibrium drop shapes and contact angles. These states can be divided into three states: (i) the moderate state, in which the contact angle is just  $90^\circ$  and is the average of the contact angles of the hydrophilic and hydrophobic stripes; (ii) the contracted state, in which the contact angle is greater than  $90^\circ$  (nearly  $110^\circ$  in this study); and (iii) the elongated state, in which the contact angle is less than  $90^\circ$  (nearly  $70^\circ$  in this study). The drops in the three states are all in mechanical equilibrium; namely, without evaporation or external force, they will remain unchanged on the horizontal substrate.

The variations of  $\theta_a$  and  $\theta_r$  with increasing  $\varphi$  for the three different states are shown in Fig. 3. In the moderate state (black stars),  $\theta_a$  linearly increases and  $\theta_r$  linearly decreases with increasing  $\varphi$ . When  $\varphi$  reaches  $15^\circ$ ,  $\theta_a$  and  $\theta_r$  almost simultaneously reach the critical values  $\theta_A$  ( $120^\circ$ ) and  $\theta_R$  ( $60^\circ$ ). The drop remains stuck on the substrate for only 0.165 s. The gray shaded region of Fig. 3 indicates that the substrate inclination is no longer increased, as the slope angle of the substrate reaches  $15^\circ$ . The whole drop starts sliding and the onset of  $\theta_a$  and  $\theta_r$  instability occurs. Therefore, the critical tilt angle in the moderate state is  $\varphi_C = 15^\circ$ .

For the contracted and elongated states (Fig. 3, red and blue circles),  $\theta_a$  increases and  $\theta_r$  decreases with increasing  $\varphi$  for  $\varphi < 6^\circ$ . When  $\varphi > 6^\circ$ , there are clear differences. For the contracted state,  $\theta_a$  first reaches the critical advancing contact angle  $\theta_A$  when  $\varphi$  increases to  $6^\circ$ , whereas  $\theta_r$  first reaches the critical receding contact angle  $\theta_R$  when  $\varphi$  increases to  $9^\circ$  for the elongated state. Differing from the moderate state, sudden instabilities of  $\theta_a$  and  $\theta_r$  occur in the contracted state (red circles) and elongated state (blue circles), respectively (Fig. 3). When  $\theta_a$  or  $\theta_r$  starts to oscillate, the other contact angle ( $\theta_r$  or  $\theta_a$ ) rapidly reaches the critical value. The reasons for the local instabilities of the front or rear end of the drop are discussed in Sec. III C.



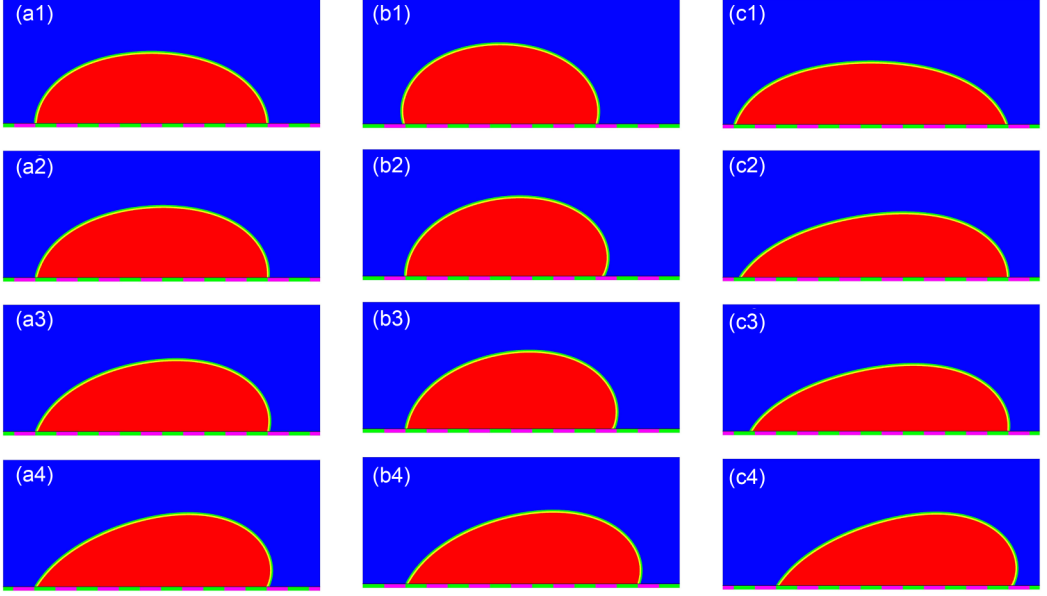


FIG. 4. Snapshots of drops on inclined planes. (a) Moderate state at (a1)  $\varphi = 0^\circ$ , (a2)  $\varphi = 5^\circ$ , (a3)  $\varphi = 9^\circ$ , and (a4)  $\varphi = 15^\circ$ . (b) Contracted state at (b1)  $\varphi = 0^\circ$ , (b2)  $\varphi = 7^\circ$ , (b3)  $\varphi = 8^\circ$ , and (b4)  $\varphi = 15^\circ$ . (c) Elongated state at (c1)  $\varphi = 0^\circ$ , (c2)  $\varphi = 9^\circ$ , (c3)  $\varphi = 11^\circ$ , and (c4)  $\varphi = 15^\circ$ .

The transformations of the drops with different initial states on inclined planes are shown in Fig. 4. In the moderate state, the drop changes from the moderate state to the hysteresis state with increasing  $\varphi$  [Fig. 4(a)]. The drop is symmetric and spans 11 stripes at  $\varphi = 0^\circ$  [Fig. 4(a1)]. The front and rear contact lines are located on the junction of stripes with different wettability. When  $\varphi$  increases step by step, the front and rear contact angles gradually change and the symmetry of the drop is broken [Figs. 4(a2)–4(a4)]. The front and rear contact lines are still pinned at the junction of the hydrophilic and hydrophobic stripes until  $\varphi = 15^\circ$ . The drop reaches the critical sliding state in Fig. 4(a4).

Unlike the moderate state, unilateral depinning is observed in the contracted and elongated states when  $\varphi$  increases step by step [Figs. 4(b) and 4(c)]. In Figs. 4(b1) and 4(c1), the drops are symmetric at  $\varphi = 0^\circ$  and the front and rear contact lines are located at the junction of the stripes. Nevertheless, they wet different numbers of stripes, namely, nine stripes for the contracted state and 13 stripes for the elongated state. Subsequently, owing to the increase of  $\varphi$ , the contact line of the drop starts to move. For the contracted state, the front contact line starts to leave the hydrophilic-hydrophobic junction and moves on the hydrophobic stripe before  $\varphi$  reaches  $8^\circ$  [Figs. 4(b2) and 4(b3)]. The front contact line slips past the hydrophobic-hydrophilic junction and the hydrophilic stripe finally stops at the next hydrophilic-hydrophobic junction after  $\varphi \geq 8^\circ$  [Fig. 4(b4)]. For the elongated state, similar motion of the rear contact line is observed [Figs. 4(c2) and 4(c4)]. In contrast, at the rear end of the contracted state and the front end of the elongated state, the contact lines are almost pinned to the original locations, but only  $\theta_r$  decreases or  $\theta_a$  increases.

For the contracted and elongated states, the sudden instabilities of the contact angle are accompanied by unilateral depinning of the contact line (Figs. 3 and 4). The unilateral depinning in the contracted state occurs earlier than that in the elongated state. The critical tilt angles are determined to be  $\varphi_A = 8^\circ$  in the contracted state and  $\varphi_R = 11^\circ$  in the elongated state (Fig. 3, circles). By comparing the three depinning behaviors of the three states, we find  $\varphi_A < \varphi_R < \varphi_C$ . This result is in agreement with the experimental results in Ref. [17], and similar results are found in Refs. [18,21].



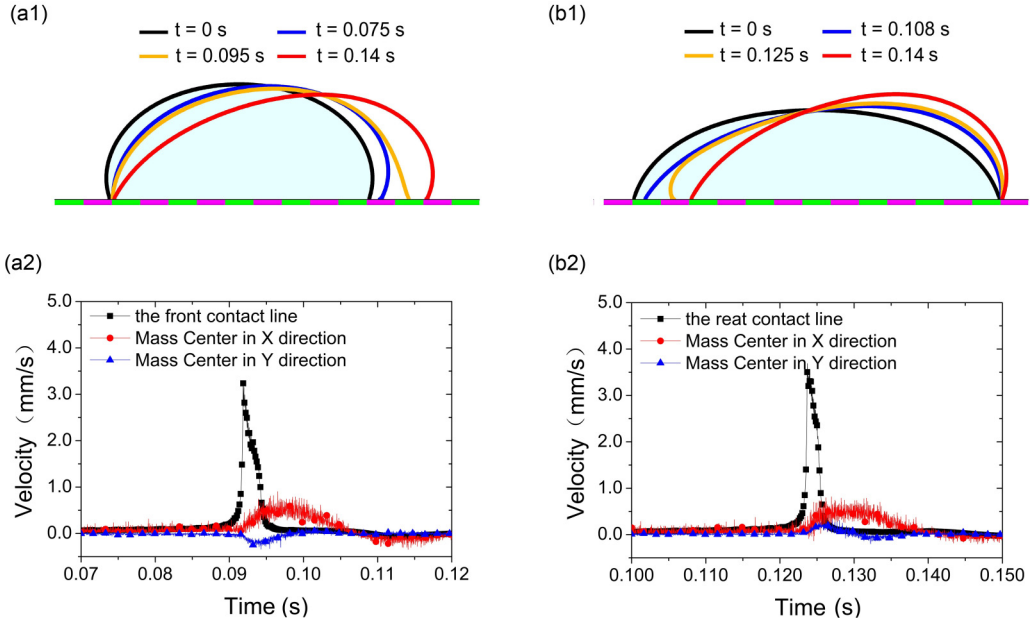


FIG. 5. Drop contours at different times (top) and time evolution of the velocity (bottom) in the unilateral depinning process: (a) contracted state and (b) elongated state.

Furthermore, after completing partial adjustment in these two cases, the drops reach critical sliding states which are similar to the moderate case [Figs. 4(b4) and 4(c4)].

To further investigate the unilateral depinning processes, the drop contours at different times and the variations of the velocities of the contact line and mass center in the contracted and elongated states are shown in Fig. 5. For the contracted state [Fig. 5(a)], the front contact line slowly moves until the slope angle increases to  $8^\circ$  ( $t = 0.075$  s). The moving distance of the front contact line is very small within the first 0.075 s [blue line in Fig. 5(a1)]. The velocities of the front contact line and mass center in the X direction are slightly above zero, whereas the velocity of the mass center in the Y direction is close to zero [see Fig. 5(a2)].

Between 0.075 and 0.095 s, the front contact line starts to rapidly slip and crosses the hydrophobic-hydrophilic boundary [yellow line in Fig. 5(a1)]. The slip is accompanied by a dramatic change of  $\theta_a$ . In addition, the velocity of the front contact line suddenly increases and reaches a peak of about 0.033 mm/s. Subsequently, it rapidly decreases to almost zero. Conversely, the velocity of the mass center in the X direction increases and the velocity of the mass center in the Y direction increases in the negative direction. The velocities of the mass center in the X and Y directions are maintained for a while, and they then return to zero [Fig. 5(a2)]. The results show that the mass center of the drop moves forward and downward. It is also observed that the drop starts to deform before the rapid slip. Local deformation mainly occurs in the front contact line region at the rapid slip, and the main deformations occur after the rapid slip.

These observations indicate that the unilateral depinning process consists of slow-moving and fast-moving stages. The depinning is in the slow-moving stage until 0.075 s, and it then changes into the fast-moving stage.

Similar contact line movement is observed in the elongated state. The major difference is that the stripes on which unilateral depinning occurs have different wettabilities. In the contracted state, a hydrophobic stripe is first crossed and then a hydrophilic stripe, whereas the order is the opposite in the elongated state, as shown in Fig. 5(b). Another difference is that the velocity change is different. The velocity change of the rear contact line occurs in less time. The velocity of the mass center in

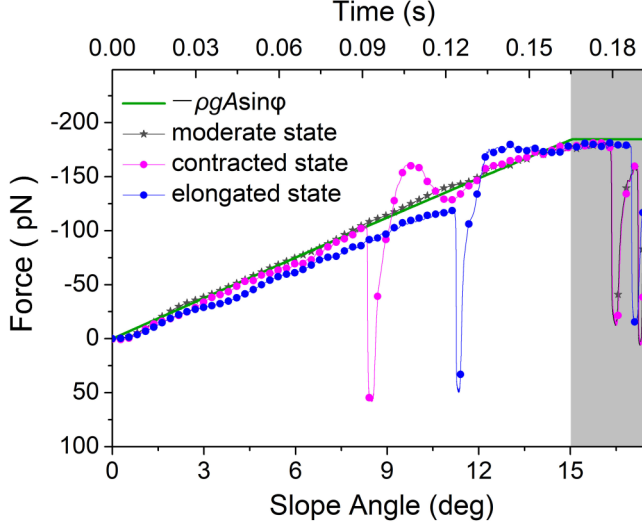


FIG. 6. Comparison of the changes of the capillary force in three drops with different initial states.

the  $Y$  direction increases in the positive direction and the mass center of the drop moves forward and upward [see Fig. 5(b)]. This is because the initial mass center of the contracted state is higher than that of the elongated state.

By considering different initial states of drop deposition, three different depinning behaviors are successfully reproduced by the LB simulations. The key observation from this group of simulation data is that the depinning behaviors of the three drops are different because the initial states are different, even though the three drops have the same volume and are on the same surface. Depinning of the front contact line first occurs in the contracted state, where  $(\theta_A + \theta_R)/2 < \theta_{\text{ini}} < \theta_A$ . In contrast, depinning of the rear contact line first occurs in the elongated state, where  $\theta_R < \theta_{\text{ini}} < (\theta_A + \theta_R)/2$ . After completing partial adjustment, the drops naturally return to the same hysteresis state because the volumes of the drops for the three cases are the same. The drops for all three cases almost simultaneously start to slide when  $\varphi$  reaches  $15^\circ$ . This implies that the contracted and elongated states first relax to the moderate state before depinning as the substrate is very slowly tilted. The results of the simulations are in good agreement with the fifth viewpoint about contact line movement in Ref. [53], the experimental results in Ref. [54], and the discussion by a bifurcation analysis in Ref. [23]. Furthermore, the results show that the depinning process consists of a slow-moving process and a fast-moving process.

### B. Analysis of the overall force balance

The state of a drop on an inclined substrate is governed by the competition between gravity and the capillary force. The gravitational force tends to deform the drop and eventually move it, whereas the capillary force attempts to prevent such drop motion. In the two-dimensional model, the force balance in directions parallel to the substrate can be expressed as [19,55]

$$\rho g A \sin \varphi = \gamma (\cos \theta_r - \cos \theta_a), \quad (16)$$

where  $\rho$  is the liquid density,  $g$  is the acceleration of gravity,  $A$  is the area of the drop,  $\varphi$  is the inclination angle of the solid substrate,  $\gamma$  is the liquid-vapor interfacial tension, and  $\theta_a$  and  $\theta_r$  are the front and rear contact angles, respectively. Because the contact angle can be calculated on the spot [41], the real-time changes of the capillary force can be obtained, as shown in Fig. 6. In the moderate state, the capillary force linearly increases step by step until  $\varphi$  reaches  $15^\circ$ . The variation trend of the magnitude is the same as the trend of the gravitational force, so the local

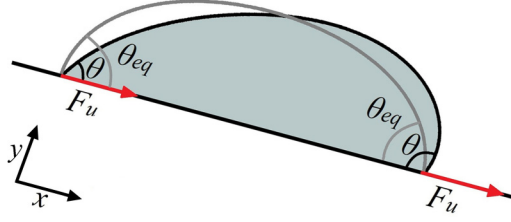


FIG. 7. Unbalanced Young's forces at the rear ( $\theta < \theta_{eq}$ ) and front ( $\theta > \theta_{eq}$ ) contact lines.

balance is maintained and results in the phenomenon of contact angle hysteresis. The gray region in Fig. 6 indicates that the substrate inclination is no longer increased as  $\varphi$  reaches  $15^\circ$ . Therefore, when the  $\varphi$  reaches critical tilt angle, the drop starts sliding and the capillary force begins to violently oscillate; the gravitational force remains the same. As reported in Refs. [12,14], the contact lines start to depin and the drop slides down when the capillary force is close to zero.

The contracted and elongated states are obviously different from the moderate state. For the contracted and elongated states, there are abrupt changes in the magnitude and direction of the capillary force at  $\varphi = 8^\circ$  and  $\varphi = 11^\circ$ , respectively. For the contracted state, the capillary force changes from  $-105$  pN to about  $56$  pN, whereas it changes from  $-118$  pN to about  $48$  pN for the elongated state. After the spikes, the balance between the gravitational and capillary force is restored before  $\varphi$  reaches  $15^\circ$  for both cases. It can be inferred that the capillary force spikes result in unilateral depinning of the drops, and it makes the drops in the critical sliding state. However, these changes do not cause the drops to slide down.

### C. Analysis of the unilateral depinning behavior of the drops

The unilateral depinning behavior was investigated in detail by observing the liquid-vapor interface motion at the microscale and analyzing the changes of the local force at the front or rear contact line.

In the contact-line region, the local force balance will change with the interface distortion. In the energy argument that leads to Young's equation, when the dynamic contact angle deviates from the equilibrium contact angle  $\theta_{eq}$ , the unbalanced Young's force would occur in the contact-line region and be dissipated because of the contact-line motion [7,26]. The unbalanced Young's force (per unit length) can be expressed as

$$F_u = \gamma(\cos \theta - \cos \theta_{eq}), \quad (17)$$

where  $\gamma$  is the liquid-vapor interfacial tension,  $\theta_{eq}$  is the equilibrium contact angle related to the surface properties, and  $\theta$  is the dynamic contact angle [7]. The unbalanced Young's force is shown in Fig. 7. When  $\theta > \theta_{eq}$ , a positive unbalanced Young's force would be generated at the front contact line, whereas when  $\theta < \theta_{eq}$ , a positive unbalanced Young's force would be generated at the rear contact line.

It is widely recognized that the contact angle is only affected by the surface components near the three-phase contact line [56–58]. The equilibrium contact angle of the heterogeneous surface is described by a modified Cassie-Baxter equation [58]:

$$\cos \theta_{eq} = r\varphi_d \cos \theta_{S1} + (1 - \varphi_d) \cos \theta_{S2}, \quad (18)$$

where  $\theta_{S1}$  and  $\theta_{S2}$  are the intrinsic equilibrium contact angles of each surface component,  $r$  is the "roughness" of the surface ( $r = 1$  for a chemically heterogeneous surface), and  $\varphi_d$  is the local areal ratio on the regions of the three-phase contact line. In the context of two-dimensional diffuse interface modeling, the liquid-vapor interface can be considered to be a cluster of isodensity lines and the thickness of the liquid-vapor interface can be described by the total length of the isodensity

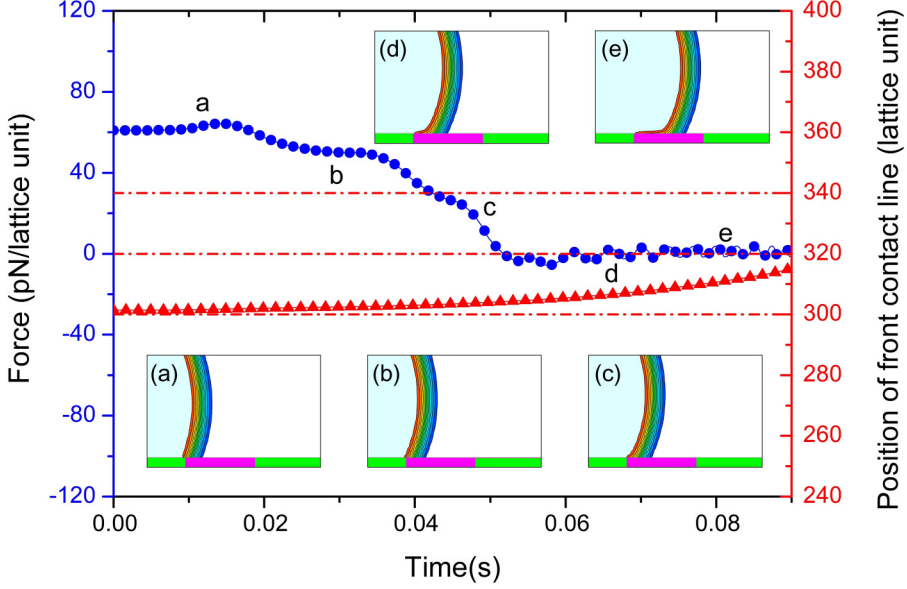


FIG. 8. Time evolution of the unbalanced Young's force (blue line) and the position of the front contact line (red line) for the contracted state in the slow-moving stage. Insets (a)–(e) show the local details of the liquid-vapor interface at the front contact line.

lines [26]. Therefore,  $\varphi_d$  and  $1 - \varphi_d$  can be replaced by the length fractions of the isodensity lines on the hydrophilic and hydrophobic stripes, respectively. When the contact line is located on the junction of the hydrophobic-hydrophilic stripes, the corresponding equilibrium contact angle can be estimated from Eq. (18). When the contact line is completely in a hydrophobic or hydrophilic stripe, the equilibrium contact angle is equal to  $120^\circ$  or  $60^\circ$ , which also obeys Eq. (18).

As discussed in Sec. III A, the depinning process can be divided into the slow-moving and fast-moving stages. In the slow-moving stage, the time evolution of the unbalanced Young's force and the position of the front contact line for the contracted state are shown in Fig. 8. The unbalanced Young's force starts at a stable value (about 60 pN/lattice unit, spot “a” in Fig. 8), but it then slowly decreases in the next 0.04 s. From insets (a)–(c) in Fig. 8, the liquid-vapor interface is more curved as the substrate slowly tilts. This interface distortion leads to a change of the unbalanced Young's force. Finally the unbalanced Young's force decreases to zero at near 0.05 s (blue circles in Fig. 8). Within the first 0.05 s, the position of the front contact line gradually moves away from 300 (the hydrophilic-hydrophobic junction, red triangles in Fig. 8). After 0.05 s, the unbalanced Young's force continues to hover around zero and the contact line is completely in a hydrophobic stripe. Insets (d) and (e) in Fig. 8 show that the contact line continues to move forward and the contact angle does not change. The results show that the front contact line is not relaxed in the initial stage of the drop. That is, before the substrate starts to tilt, the unbalanced Young's force is balanced by the resistance of the substrate. After the substrate slowly tilts, the local force balance is maintained by the unbalanced Young's force and the resistance of the substrate. In this stage, the contact line movement is governed by the unbalanced Young's force and the resistance of the substrate.

In the elongated state (Fig. 9), the movement of the contact line and the variation of the unbalanced Young's force on the rear contact line are similar to those in the contracted state. The initial value of the unbalanced Young's force exceeds 80 pN/lattice unit, which is larger than that of the contracted state. This indicates that the resistance in the rear contact line of the elongated state is greater than that in the front contact line of the contracted state. Therefore, it takes more

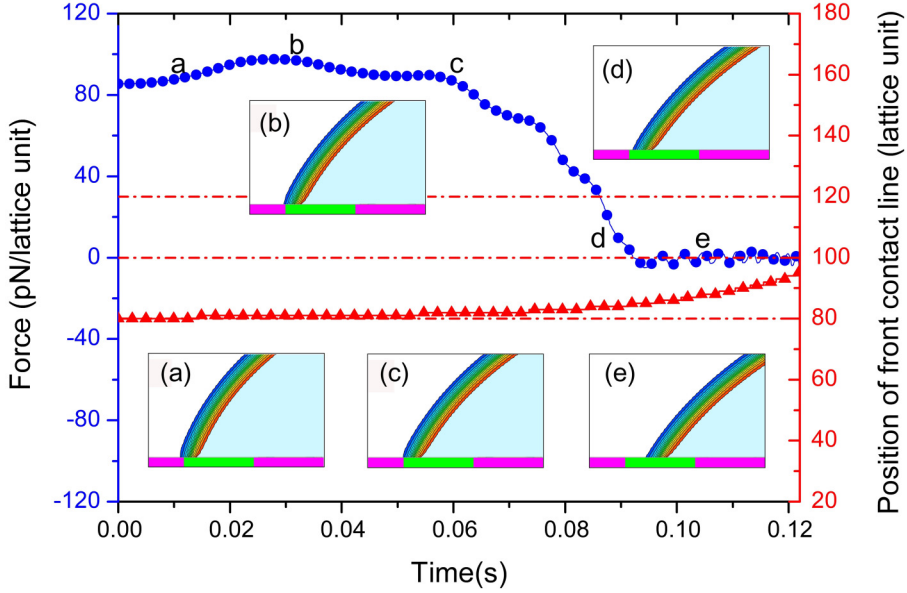


FIG. 9. Time evolution of the unbalanced Young's force (blue line) and the position of the rear contact line (red line) for the elongated state in the slow-moving stage. Insets (a)–(e) show the local details of the liquid-vapor interface at the rear contact line.

time to move away from the junction of the hydrophobic-hydrophilic stripe. This can explain why depinning of the elongated state occurs later than that of the contracted state.

In the fast-moving stage, the time evolution of the unbalanced Young's force and the position of the front contact line for the contracted state are shown in Fig. 10. The front contact line passes over the hydrophobic-hydrophilic boundary, slips through the hydrophilic stripe, and sticks on the hydrophilic-hydrophobic boundary within 0.006 s (red triangles in Fig. 10). In just 0.006 s, the unbalanced Young's force undergoes up-and-down fluctuations twice (blue circles in Fig. 10). In the first fluctuation, the front contact line initially reaches the hydrophobic-hydrophilic boundary and is hampered [inset (a) in Fig. 10]. As the slope angle continues to increase, the liquid-vapor interface deforms and causes the unbalanced Young's force to rapidly increase. The change of the force causes the velocity of the front contact line to rapidly increase [see Fig. 5(a2)]. The front contact line is pulled through the junction [spot “b” and inset (b) in Fig. 10]. Subsequently, because of a rapid slip of the contact line, the dynamic contact angle fails to keep up with the change [Fig. 10(c)]. When the dynamic contact angle is less than the equilibrium contact angle, the unbalanced Young's force turns in the opposite direction. Between the two fluctuations, the unbalanced Young's force remains stable at about 30 pN/lattice unit and the front contact line steadily slips through the hydrophilic stripe [inset (d) in Fig. 10]. In another fluctuation, when the front contact line reaches 340, the unbalanced Young's force achieves the negative peak value [spot “e” and inset (e) in Fig. 10]. The force causes the velocity of the front contact line to decrease to zero. Subsequently, even if the unbalanced Young's force keeps increasing to push the contact line ahead, the position of the front contact line is still blocked at 340 (Fig. 10). This is because the front contact encounters the resistance of the substrate again. The unbalanced Young's force is balanced by the resistance of the substrate at the three-phase contact point. However the interface is bent,  $\theta_a$  continues to increase, and  $\theta_a$  is finally close to the critical value  $\theta_A$ .

Time evolution of the unbalanced Young's force and position of rear contact line for the elongated state in the fast-moving stage are shown in Fig. 11. The difference between the elongated state and contracted state is that the first fluctuation of the unbalanced Young's force is more intense whereas

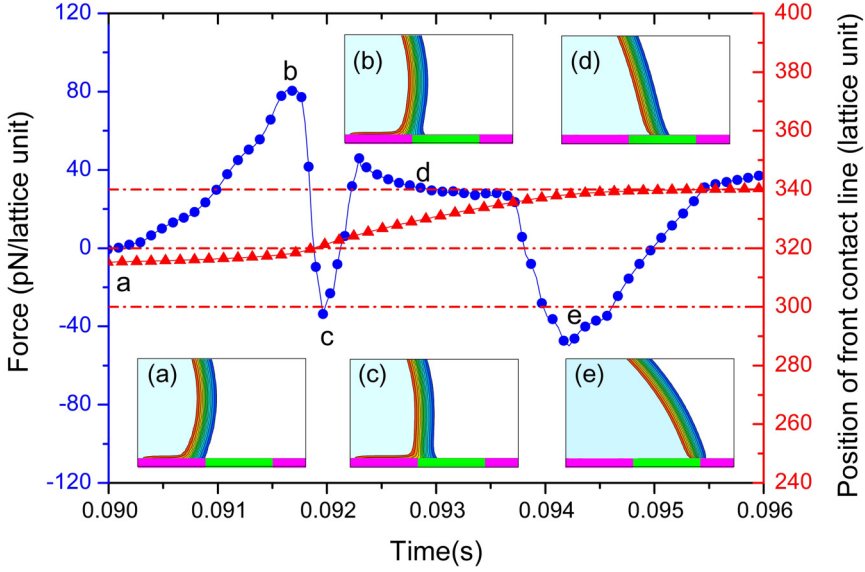


FIG. 10. Time evolution of the unbalanced Young's force (blue line) and position of the front contact line (red line) for the contracted state in the fast-moving stage. Insets (a)–(e) show the local details of the liquid-vapor interface at the front contact line.

the second fluctuation is less intense for the elongated state (Fig. 11). Thus, in Fig. 5, the velocity of the contact line increases faster and also falls faster than those of the contracted state, and the whole fast-moving process takes less time. The main reason is that the wettability of the region where the

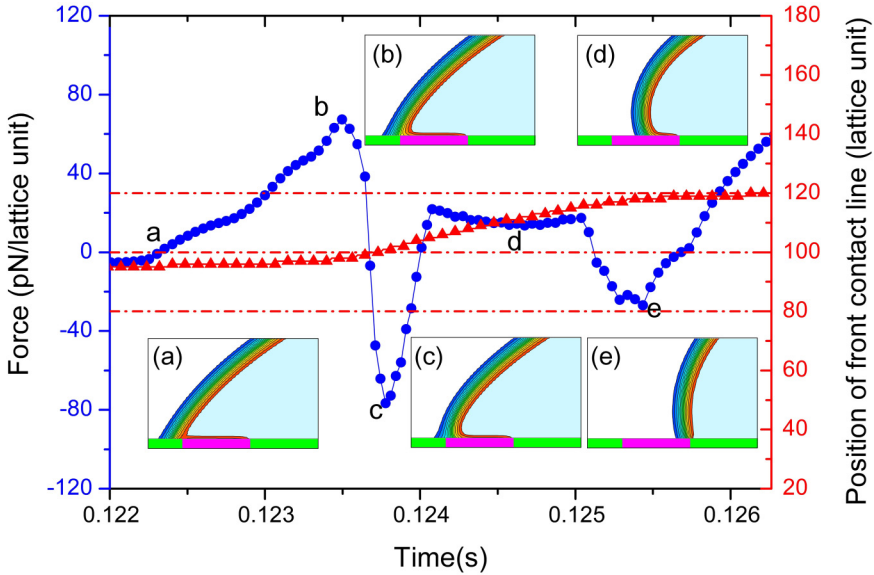


FIG. 11. Time evolution of the unbalanced Young's force (blue line) and position of the rear contact line (red line) for the elongated state in the fast-moving stage. Insets (a)–(e) show the local details of the liquid-vapor interface at the rear contact line.



depinning of the elongated state occurs is more hydrophobic than that of the contracted state. The movement of the contact line on the hydrophobic stripe shortens the time of the whole process.

By observing the details of the depinning process, the surface properties of the region of the contact line affect the duration of the slow-moving stage and the slip velocity of the contact line. In the slow-moving stage, the local force balance is maintained by the unbalanced Young's force and the resistance of the substrate. In the fast-moving stage, an intense fluctuation of the unbalanced Young's force leads to rapid slip of the contact line and breaks the local force balance. Ultimately, it causes variation of the capillary force.

#### IV. CONCLUSIONS

In this study, we have investigated the depinning behavior of drops with different initial states on a chemically heterogeneous surface using the multiphase LBM driven by the chemical potential. Three different initial states of the drop were considered: the moderate state, the contracted state, and the elongated state. First, the depinning behavior of these three drops on chemically heterogeneous surfaces was observed. When the initial drop shape is the contracted or elongated state, unilateral depinning occurs at  $\theta_a$  or  $\theta_r$  accompanied by a rapid slip of the contact line on the hydrophilic or hydrophobic stripe. A unilateral depinning process consisting of a slow-moving process and a fast-moving process occurs. After the fast-moving process, the drops naturally return to a similar critical sliding state because the volumes of the drops are the same in the three cases. The critical slope angles of the depinning are in the order  $\varphi_A < \varphi_R < \varphi_C$ , which is consistent with experimental results. The capillary force was then analyzed by the real-time contact angles obtained by simulations. The results show that there is a basic balance between the capillary force and gravitational force, and the unilateral depinning of the drop is accompanied by a sudden increase in the capillary force. Furthermore, the effect of heterogeneous patterning on the partial depinning behavior was determined by observing the movement of the contact line and analyzing the variations of the local unbalanced Young's force. The results show that the contact line is not relaxed in the initial stage for the contracted and elongated drops. The unbalanced Young's force is balanced by the resistance of the substrate in the slow-moving stage, whereas the fluctuations of the force result in a sudden velocity change in the front or rear contact line in the fast-moving stage. Because a diffuse interface is used in our simulations, it is required that the stripe width is larger than the thickness of the diffuse interface. Three-dimensional analyses and simulations about drop motion on various patterned surfaces have been performed by different methods, such as thin-film models [25] and LBM [14]. Based on the dynamics contact angle, three-dimensional analyses and simulations about drop depinning will be performed in future work.

The original data for the figures are publicly available through figshare [59].

#### ACKNOWLEDGMENTS

This work was supported by the National Natural Science Foundation of China (Grants No. 11862003 and No. 81860635), the Key Project of Guangxi Natural Science Foundation (Grant No. 2017GXNSFDA198038), the Guangxi Natural Science Foundation (Grant No. 2018GXNS-FAA281302), Guangxi "Bagui Scholar" Teams for Innovation and Research Project, and Guangxi Collaborative Innovation Center of Multi-source Information Integration and Intelligent Processing.

- 
- [1] A. A. Darhuber and S. M. Troian, Principles of microfluidic actuation by modulation of surface stresses, *Annu. Rev. Fluid Mech.* **37**, 425 (2005).
  - [2] R. Blossey, Self-cleaning surfaces—virtual realities, *Nat. Mater.* **2**, 301 (2003).



- [3] K. Rykaczewski, A. T. Paxson, M. Staymates, M. L. Walker, X. Sun, S. Anand, S. Srinivasan, G. H. McKinley, J. Chinn, J. H. J. Scott, and K. K. Varanasi, Dropwise condensation of low surface tension fluids on omniphobic surfaces, *Sci. Rep.* **4**, 4158 (2014).
- [4] K.-C. Park, S. S. Chhatre, S. Srinivasan, R. E. Cohen, and G. H. McKinley, Optimal design of permeable fiber network structures for fog harvesting, *Langmuir* **29**, 13269 (2013).
- [5] N. Gao, F. Geyer, D. W. Pilat, S. Wooh, D. Vollmer, and R. Berger, How drops start sliding over solid surfaces, *Nat. Phys.* **14**, 191 (2018).
- [6] J. Park and S. Kumar, Droplet sliding on an inclined substrate with a topographical defect, *Langmuir* **33**, 7352 (2017).
- [7] Y. Sui, H. Ding, and P. D. M. Spelt, Numerical simulations of flows with moving contact lines, *Annu. Rev. Fluid Mech.* **46**, 97 (2014).
- [8] G. Mistura and M. Pierno, Drop mobility on chemically heterogeneous and lubricant-impregnated surfaces, *Adv. Phys.: X* **2**, 591 (2017).
- [9] M. Morita, T. Koga, H. Otsuka, and A. Takahara, Macroscopic-wetting anisotropy on the line-patterned surface of fluoroalkylsilane monolayers, *Langmuir* **21**, 911 (2005).
- [10] S. Suzuki, A. Nakajima, K. Tanaka, M. Sakai, A. Hashimoto, N. Yoshida, Y. Kameshima, and K. Okada, Sliding behavior of water droplets on line-patterned hydrophobic surfaces, *Appl. Surf. Sci.* **254**, 1797 (2008).
- [11] S. Varagnolo, D. Ferraro, P. Fantinel, M. Pierno, G. Mistura, G. Amati, L. Biferale, and M. Sbragaglia, Stick-Slip Sliding of Water Drops on Chemically Heterogeneous Surfaces, *Phys. Rev. Lett.* **111**, 066101 (2013).
- [12] M. Sbragaglia, L. Biferale, G. Amati, S. Varagnolo, D. Ferraro, G. Mistura, and M. Pierno, Sliding drops across alternating hydrophobic and hydrophilic stripes, *Phys. Rev. E* **89**, 012406 (2014).
- [13] Y. X. Wang, M. P. Jian, H. Y. Liu, and X. W. Zhang, Anisotropic wetting of droplets on stripe-patterned chemically heterogeneous surfaces: Effect of length ratio and deposition position, *Langmuir* **35**, 4387 (2019).
- [14] S. Varagnolo, V. Schiocchet, D. Ferraro, M. Pierno, G. Mistura, M. Sbragaglia, A. Gupta, and G. Amati, Tuning drop motion by chemical patterning of surfaces, *Langmuir* **30**, 2401 (2014).
- [15] C. S. Lin, S. Chen, L. L. Xiao, and Y. Liu, Tuning drop motion by chemical chessboard-patterned surfaces: A many-body dissipative particle dynamics study, *Langmuir* **34**, 2708 (2018).
- [16] U. Thiele and E. Knobloch, On the depinning of a driven drop on a heterogeneous substrate, *New J. Phys.* **8**, 313 (2006).
- [17] V. Berejnov and R. E. Thorne, Effect of transient pinning on stability of drops sitting on an inclined plane, *Phys. Rev. E* **75**, 066308 (2007).
- [18] T. H. Chou, S. J. Hong, Y. J. Sheng, and H. K. Tsao, Drops sitting on a tilted plate: Receding and advancing pinning, *Langmuir* **28**, 5158 (2012).
- [19] M. J. Santos, S. Velasco, and J. A. White, Simulation analysis of contact angles and retention forces of liquid drops on inclined surfaces, *Langmuir* **28**, 11819 (2012).
- [20] S. Bommer, H. Scholl, R. Seemann, K. Kanhaiya, V. Sheraton M, and N. Verma, Depinning of drops on inclined smooth and topographic surfaces: Experimental and lattice Boltzmann model study, *Langmuir* **30**, 11086 (2014).
- [21] N. Janardan and M. V. Panchagnula, Effect of the initial conditions on the onset of motion in sessile drops on tilted plates, *Colloids Surf. A* **456**, 238 (2014).
- [22] J. A. White, M. J. Santos, M. A. Rodríguez-Valverde, and S. Velasco, Numerical study of the most stable contact angle of drops on tilted surfaces, *Langmuir* **31**, 5326 (2015).
- [23] D. Herde, U. Thiele, S. Herminghaus, and M. Brinkmann, Driven large contact angle droplets on chemically heterogeneous substrates, *Europhys. Lett.* **100**, 16002 (2012).
- [24] M. A. Sarshar, Y. Jiang, W. Xu, and C. H. Choi, Depinning force of a receding droplet on pillared superhydrophobic surfaces: Analytical models, *J. Colloid Interface Sci.* **543**, 122 (2019).
- [25] P. H. Ph. Beltrame and U. Thiele, Depinning of three-dimensional drops from wettability defects, *Europhys. Lett.* **86**, 24006 (2009).

- [26] Q. Li, P. Zhou, and H. J. Yan, Pinning-depinning mechanism of the contact line during evaporation on chemically patterned surface: A lattice Boltzmann study, *Langmuir* **32**, 9389 (2016).
- [27] M. Liu and X. P. Chen, Numerical study on the stick-slip motion of contact line moving on heterogeneous surfaces, *Phys. Fluids* **29**, 082102 (2017).
- [28] C. Lee, S. Lyu, J. W. Park, and W. Hwang, Lattice Boltzmann simulation of the movement of droplets on stripe-patterned surfaces having different wettability, *Adv. Eng. Software* **91**, 44 (2016).
- [29] B. H. Wen, Z. R. Qin, C. Y. Zhang, and H. P. Fang, Thermodynamic-consistent lattice Boltzmann model for nonideal fluids, *Europhys. Lett.* **112**, 44002 (2015).
- [30] B. H. Wen, X. Zhou, B. He, C. Y. Zhang, and H. P. Fang, Chemical-potential-based lattice Boltzmann method for nonideal fluids, *Phys. Rev. E* **95**, 063305 (2017).
- [31] J. H. Snoeijer and B. Andreotti, Moving contact lines: Scales, regimes, and dynamical transitions, *Annu. Rev. Fluid Mech.* **45**, 269 (2013).
- [32] D. M. Anderson, G. B. McFadden, and A. A. Wheeler, Diffuse interface methods in fluid mechanics, *Annu. Rev. Fluid Mech.* **30**, 139 (1998).
- [33] L. Chen, Q. Kang, Y. Mu, Y.-L. He, and W.-Q. Tao, A critical review of the pseudopotential multiphase lattice Boltzmann model: Methods and applications, *Int. J. Heat Mass Transfer* **76**, 210 (2014).
- [34] Q. Li, K. H. Luo, Q. J. Kang, Y. L. He, Q. Chen, and Q. Liu, Lattice Boltzmann methods for multiphase flow and phase-change heat transfer, *Prog. Energy Combust. Sci.* **52**, 62 (2016).
- [35] B. H. Wen, C. Y. Zhang, Y. S. Tu, C. L. Wang, and H. P. Fang, Galilean invariant fluid-solid interfacial dynamics in lattice Boltzmann simulations, *J. Comput. Phys.* **266**, 161 (2014).
- [36] S. Brandon and A. Marmur, Simulation of contact angle hysteresis on chemically heterogeneous surfaces, *J. Colloid Interface Sci.* **183**, 351 (1996).
- [37] S. Brandon, A. Wachs, and A. Marmur, Simulated contact angle hysteresis of a three-dimensional drop on a chemically heterogeneous surface: A numerical example, *J. Colloid Interface Sci.* **191**, 110 (1997).
- [38] S. Brandon, N. Haimovich, E. Yeager, and A. Marmur, Partial wetting of chemically patterned surfaces: The effect of drop size, *J. Colloid Interface Sci.* **263**, 237 (2003).
- [39] A. Marmur, Equilibrium contact angles: Theory and measurement, *Colloids Surf. A* **116**, 55 (1996).
- [40] B. Wen, L. Zhao, W. Qiu, Y. Ye, and X. Shan, Chemical-potential multiphase lattice Boltzmann method with superlarge density ratios, *Phys. Rev. E* **102**, 013303 (2020).
- [41] B. H. Wen, B. F. Huang, Z. R. Qin, C. L. Wang, and C. Y. Zhang, Contact angle measurement in lattice Boltzmann method, *Comput. Math. Appl.* **76**, 1686 (2018).
- [42] S. Y. Chen and G. D. Doolen, Lattice Boltzmann method for fluid flows, *Annu. Rev. Fluid Mech.* **30**, 329 (1998).
- [43] C. K. Aidun and J. R. Clausen, Lattice-Boltzmann method for complex flows, *Annu. Rev. Fluid Mech.* **42**, 439 (2010).
- [44] Y. H. Qian, D. d'Humières, and P. Lallemand, Lattice BGK models for Navier-Stokes equation, *Europhys. Lett.* **17**, 479 (1992).
- [45] P. Lallemand and L. S. Luo, Theory of the lattice Boltzmann method: Dispersion, dissipation, isotropy, Galilean invariance, and stability, *Phys. Rev. E* **61**, 6546 (2000).
- [46] I. V. Karlin, A. Ferrante, and H. C. Ottinger, Perfect entropy functions of the lattice Boltzmann method, *Europhys. Lett.* **47**, 182 (1999).
- [47] R. J. Shipley and B. Widom, *Molecular Theory of Capillarity* (Clarendon, Oxford, 1982).
- [48] M. R. Swift, W. R. Osborn, and J. M. Yeomans, Lattice Boltzmann Simulation of Nonideal Fluids, *Phys. Rev. Lett.* **75**, 830 (1995).
- [49] D. Jamet, D. Torres, and J. U. Brackbill, On the theory and computation of surface tension: The elimination of parasitic currents through energy conservation in the second-gradient method, *J. Comput. Phys.* **182**, 262 (2002).
- [50] H. W. Zheng, C. Shu, and Y. T. Chew, A lattice Boltzmann model for multiphase flows with large density ratio, *J. Comput. Phys.* **218**, 353 (2006).
- [51] R. Benzi, L. Biferale, M. Sbragaglia, S. Succi, and F. Toschi, Mesoscopic modelling of heterogeneous boundary conditions for microchannel flows, *J. Fluid Mech.* **548**, 257 (2006).
- [52] C. Semprebona and M. Brinkmann, On the onset of motion of sliding drops, *Soft Matter* **10**, 3325 (2014).

- [53] L. Gao and T. J. McCarthy, Contact angle hysteresis explained, [Langmuir](#) **22**, 6234 (2006).
- [54] A. Y. Fadeev and T. J. McCarthy, Trialkylsilane monolayers covalently attached to silicon surfaces: Wettability studies indicating that molecular topography contributes to contact angle hysteresis, [Langmuir](#) **15**, 3759 (1999).
- [55] G. MacDougall and C. Ockrent, Surface energy relations in liquid/solid systems I. The adhesion of liquids to solids and a new method of determining the surface tension of liquids, [Proc. R. Soc. London, Ser. A](#) **180**, 151 (1942).
- [56] P. S. H. Forsberg, C. Priest, M. Brinkmann, R. Sedev, and J. Ralston, Contact line pinning on microstructured surfaces for liquids in the Wenzel state, [Langmuir](#) **26**, 860 (2010).
- [57] L. Gao and T. J. McCarthy, Wetting  $101^\circ$ , [Langmuir](#) **25**, 14105 (2009).
- [58] W. Choi, A. Tuteja, J. M. Mabry, R. E. Cohen, and G. H. McKinley, A modified Cassie–Baxter relationship to explain contact angle hysteresis and anisotropy on non-wetting textured surfaces, [J. Colloid Interface Sci.](#) **339**, 208 (2009).
- [59] B. He, B. H. Wen, C. Y. Qin, and S. H. Zhou, Data for “Analysis of depinning behavior of drop on chemically heterogeneous surface” (2020), <https://dx.doi.org/10.6084/m9.figshare.12894509>.